

# Large-eddy simulation of large-scale structures in long channel flow

D. CHUNG AND B. J. McKEON†

Graduate Aerospace Laboratories, California Institute of Technology, Pasadena, CA 91125,  
USA  
dchung@caltech.edu

(Received ?? and in revised form ??)

We investigate statistics of large-scale structures from large-eddy simulation (LES) of turbulent channel flow at friction Reynolds numbers  $Re_\tau = 2\text{k}$  and  $200\text{k}$ . To properly capture the behaviour of large-scale structures, the channel length is chosen to be 96 times the channel half-height. In agreement with experiments, these large-scale structures are found to give rise to an apparent amplitude modulation of the underlying small-scale fluctuations. This effect is explained in terms of the phase relationship between the large- and small-scale activity. The shape of the dominant large-scale structure is investigated by conditional averages based on the large-scale velocity, determined using a filter width equal to the channel half-height. The conditioned field demonstrates coherence on a scale of several times the filter width, and the small-scale–large-scale relative phase difference increases away from the wall, passing through  $\pi/2$  in the overlap region of the mean velocity before approaching  $\pi$  further from the wall. We also found that, near the wall, the convection velocity of the large-scales departs slightly, but unequivocally, from the mean velocity.

---

## 1. Introduction

Recent studies (Kim & Adrian 1999; Morrison, McKeon, Jiang & Smits 2004; Guala, Himmema & Adrian 2006; Monty, Stewart, Williams & Chong 2007; Hutchins & Marusic 2007*b,a*; Mathis, Hutchins & Marusic 2009) have confirmed earlier observations (Favre, Gaviglio & Dumas 1967; Kovaszny, Kibens & Blackwelder 1970) of very long large-scale structures in the wall region of boundary layers, channels and pipes. These structures are marked by streamwise-elongated, alternating low- and high-momentum, meandering streaks, with length  $10\delta$  (Kim & Adrian 1999; Morrison *et al.* 2004),  $8\text{--}16\delta$  (Guala *et al.* 2006),  $25\delta$  (Monty *et al.* 2007),  $6\delta$  (Hutchins & Marusic 2007*b*),  $20\delta$  (Hutchins & Marusic 2007*a*) and width  $0.3\text{--}0.5\delta$  (Mathis *et al.* 2009), where  $\delta$  is the boundary layer thickness, channel half-height or pipe diameter. See Monty *et al.* (2009) for a description of the differences between the characteristics of these large structures in the different canonical flows. The bursting period of these structures,  $6\delta/U$ , where  $U(z)$  is the mean velocity, was already noted some decades ago, along with the long tails of the streamwise velocity auto-correlations, see review by Cantwell (1981). The dynamical significance of these large-scale structures can be seen in a scale decomposition of relative energy content, as measured by the premultiplied one-dimensional longitudinal spectrum  $\kappa_x E_{uu}$  plotted against the log streamwise wavelength,  $\log \lambda_x$ , where  $\lambda_x = 2\pi/\kappa_x$  (equal area under the curve implies equal energy contribution). For a boundary layer at friction Reynolds number  $Re_\tau = 7.3\text{k}$  (Hutchins & Marusic 2007*b*), the signature of these

† Email address for correspondence: mckeon@caltech.edu

structures are related to the outer peak in  $\kappa_x E_{uu}$  found at  $(z/\delta, \lambda_x/\delta) = (0.06, 6)$ . It has been proposed that the wall-normal location of this peak is located at the middle of the log layer,  $z^+ \propto Re_\tau^{1/2}$  or  $Re_\tau^{3/4}$  (Mathis *et al.* 2009) (the choice of scaling depends on whether the lower limit of the log law is Reynolds number dependent), where  $z$  is the height from the wall and the superscript  $+$  indicates scaling in wall units: the friction velocity  $u_\tau$  and kinematic viscosity  $\nu$ . However the scaling remains somewhat ambiguous.

The large-scale structures were found (Bandyopadhyay & Hussain 1984; Mathis *et al.* 2009) to modulate the amplitudes of superimposed small-scale fluctuations. To test this idea, these authors first split the streamwise velocity into large- and small-scale components via a filter at  $\lambda_x/\delta = U(z)/(f\delta)$ , and then used either a filtered and rectified small-scale signal or the Hilbert-transform to determine the envelope for the small-scale fluctuations, finally forming the correlation coefficient between the large-scale fluctuations and the low-pass filtered envelope of the small-scale fluctuations. They found that, near the wall, large-scale high-speed regions carry intense superimposed small-scale fluctuations, but this correlation is reversed above a height that decreases in outer units with  $Re_\tau$ . We shall attempt to reproduce these features presently.

The footprint of structures centred far from the wall provides an obvious challenge in terms of determining appropriate convection velocities across the range of turbulent scales, with particular importance for obtaining the correct wavenumber spectra from temporal frequency spectra obtained by, for example, hot-wire anemometry. It has been known for some time that convection velocities deviate from the local mean in the near-wall region, (e.g. Krogstad *et al.* 1998). The common practice is to use Taylor’s frozen-turbulence hypothesis to map from the frequency to the wavenumber domain, that is to use the assumption that all structures at a given wall distance  $z$  convect at the same scale-independent mean velocity  $U(z)$ . It was shown from a particle image velocimetry (PIV) experiment (Dennis & Nickels 2008) that this is indeed good approximation at  $z/\delta = 0.16$  for a  $Re_\theta = 4.7\text{k}$  boundary layer, at least for scales smaller than their field of view,  $3.2\delta$  in space and  $6.3\delta/U$  in time. However note that this wall-normal distance is sufficiently far from the wall that it is beyond the large-scale energy peak, such that any convection velocity questions are likely insignificant because of the low shear in the outer region. With a field of view larger than  $20\delta \times 20\delta/U$  and height down to  $z/\delta = 0.049$ , we revisit the question of whether the footprint of the large-scale structures, having centres further from the wall, still convect at the local mean velocity near the wall.

To properly assess the dynamics of these long structures, reported to reach up to  $25\delta$  (Monty *et al.* 2007), we use large-eddy simulation (LES) coupled with a wall model (Chung & Pullin 2009). This investigation is ideally suited to the present wall modelled LES since its cost depends only on the number of ‘large eddies’, which, for a channel, is Reynolds number independent. In contrast, the fully resolved direct numerical simulation (DNS) is prohibitively expensive. For reference, the most ambitious DNS of a channel flow to date is the  $Re_\tau = 2\text{k}$  simulation (Hoyas & Jiménez 2006) in an  $L_x/\delta = 8\pi \approx 25$  channel, where  $L_x$  is the streamwise length; a DNS investigation at higher  $Re_\tau$  and larger  $L_x$  of these large-scale structures is not yet possible. Of course, the use of LES comes at the cost of subgrid-scale (SGS) modelling, wall modelling and numerical errors, but LES is much faster (hours for simulation, minutes for post-processing) than DNS and experiments; we hope that a controlled application of the present LES combined with experience in the subject may shed some light on the physics of these large-scale structures.

Details of the simulations are given in § 2 and discussion of observations are found in § 3 before we conclude in § 4.

Run	$Re_\tau$	$L_x/\delta$	$L_y/\delta$	$h_0^+$	$\Delta_x/\delta$	$\Delta_t u_\tau/\delta$	$N_x$	$N_y$	$N_z$	$N_t$	$TU_c/L_x$
G1	2k	95	7.9	15	0.17	0.006	576	48	48	72000	110
H3	200k	96	8.0	750	0.083	0.002	1152	96	96	15800	12
G1b	2k	95	7.9	15	0.17	0.006	576	48	48	22000	34

TABLE 1. LES parameters for long channel flows. Channel-transit times based on data-recording period  $T$  and centreline velocity  $U_c$ .

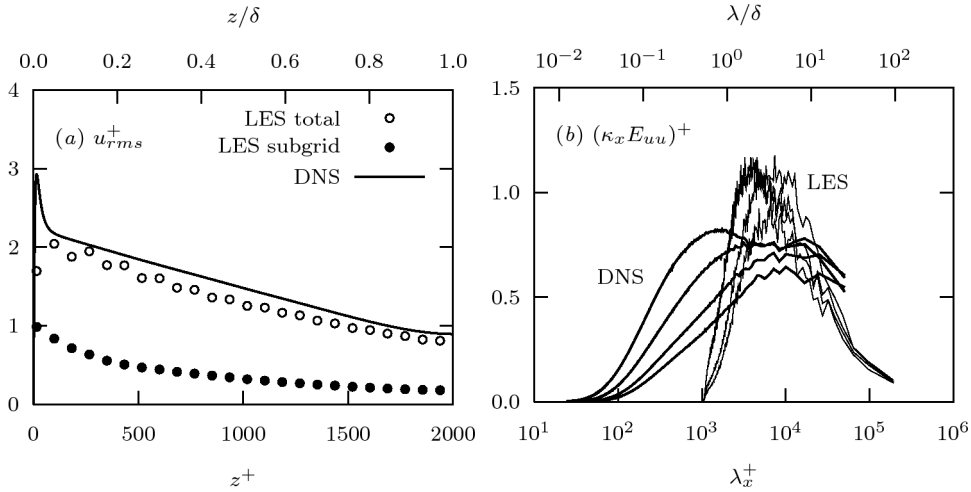


FIGURE 1. Comparison between DNS data of Hoyas & Jiménez (2006) and present  $Re = 2k$  channel flow LES, run G1b (table 1). Spectra at  $z/\delta = 0.049, 0.090, 0.17, 0.26 \Leftrightarrow z^+ = 98, 180, 350, 510$  (ordered in decreasing energy).

## 2. Simulation details

As full details of the LES, including the numerical method and SGS model, are given by Chung & Pullin (2009), we only highlight the important points here. We solve the filtered Navier–Stokes equations for the LES velocity field  $\bar{\mathbf{u}}$  using the stretched-spiral vortex SGS model (Misra & Pullin 1997; Voelkl *et al.* 2000). To circumvent the prohibitive cost of resolving the near-wall region (Chapman 1979),  $z < h_0$ , we use a wall model (Chung & Pullin 2009) that supplies off-wall slip-velocity boundary conditions at  $h_0$  to the interior LES, operating in  $h_0 < z < 2\delta - h_0$ , where  $z = 0, 2\delta$  locates the walls. Presently, we fix  $h_0 = 0.18 \Delta_z$ , and the slip velocity is calculated using a wall model comprising 1) an evolution equation for the wall shear stress derived from assuming local inner scaling for the streamwise momentum equation and 2) an extended form of the stretched-vortex SGS model that provides a local log relation along with a dynamic estimate for the local Kármán constant.

The parameters for the three LES runs are given in table 1. The grid is uniform,  $\Delta_x = \Delta_y = 4\Delta_z$ , throughout the simulation domain. To capture the physics of long large-scale structures, we use long a channel,  $L_x/\delta \approx 96$ , and the statistics are taken over  $T$  channel-transit times.

It was shown (Chung & Pullin 2009) that the LES-predicted statistics from the  $Re = 2k$  case, including means, turbulent intensities and spectra, compare reasonably well with the DNS of Hoyas & Jiménez (2006). We show the root-mean-square (r.m.s.) of the streamwise velocity fluctuations and the LES-resolved spectra in figure 1. The points

in 1(a) correspond to actual discretization points. Even though the total (subgrid plus resolved) r.m.s. is within 90% of the DNS result, its spectra plotted in energy-content form overpredicts the DNS spectra by about 20%. (Note, however, that the comparison between experimental channel flow data and DNS has revealed a similar trend, with the experimental premultiplied spectra at large wavelengths in the overlap layer being up to order 10% larger than the equivalent DNS values (Monty & Chong 2009).) As such, the results presented here should be viewed as approximate, despite capturing energy at significantly larger wavelengths. On the other hand, the physics reported here can be seen as robust features of wall turbulence if they are also observed elsewhere. We note that the peak value,  $(\kappa_x E_{uu})^+ \approx 1$  at  $z/\delta = 0.090$ ,  $\lambda/\delta \approx 6$  (figure 1) is within the range of the peak values from boundary layer spectra for  $Re_\tau = 1.0\text{--}7.3\text{ k}$  (see figure 9 of Hutchins & Marusic (2007a)). We interpret the LES results as a model of the real flow, and emphasize that  $Re_\tau = 200\text{k}$  is far out of the reach of current DNS approaches.

In order to compute correlations based on temporal averaging, a numerical rake in runs G1 and H3, fixed in streamwise–spanwise location, is set up to record the LES velocity  $\bar{u}$  and its modelled subgrid fluctuations  $T_{xx}$  ( $\equiv \overline{uu} - \bar{u}\bar{u}$ ) at the wall-normal locations  $z = n_z \Delta_z$  ( $n_z = 0, 1, \dots, N_z$ ) and time steps  $t = n_t \Delta_t$  ( $n_t = 0, 1, \dots, N_t - 1$ ). Analogous correlations based on spatial averages are also computed from these runs from a snapshot in time.

The only difference between runs G1 and G1b is the recorded data. For the latter, the three-dimensional data set,  $\bar{u}(n_x \Delta_x, y, n_z \Delta_z, n_t \Delta_t)$ , is recorded at fixed  $y$ , for  $n_x = 0, 1, \dots, 575$ ,  $n_z = 0, 1, \dots, 48$  and  $n_t = 0, 1, \dots, 21999$ , where  $\Delta_x/\delta = 0.17$ ,  $\Delta_z/\delta = 0.041$  and  $\Delta_t u_\tau/\delta = 0.006$ .

Presently,  $x$ ,  $y$  and  $z$  respectively denote the streamwise, spanwise and wall-normal directions; the velocity components,  $u$ ,  $v$  and  $w$ , are defined accordingly.

### 3. Discussion of observations

We present observations of the LES velocity fields, with emphasis on the large scales.

#### 3.1. Convection velocities from spatio-temporal spectra

We begin by using the somewhat unique combination of spatial and temporal data available in this study to investigate the validity of Taylor’s hypothesis. Given the autocorrelation of the streamwise velocity fluctuations,

$$R(\rho, \tau) = \langle u'(x, t) u'(x + \rho, t + \tau) \rangle, \quad (3.1)$$

where  $\rho$  is the streamwise separation;  $\tau$  is the time delay; and  $u \equiv U + u'$  such that  $\langle u' \rangle = 0$ , we define the spatio-temporal spectrum  $\Psi(\kappa, \omega)$  as the Fourier transform of  $R(\rho, \tau)$ . That is, together they form the Fourier transform pair, given by

$$\begin{aligned} \Psi(\kappa, \omega) &= \frac{1}{(2\pi)^2} \int_{-\infty}^{\infty} \int_{-\infty}^{\infty} R(\rho, \tau) e^{-i(\kappa\rho - \omega\tau)} d\rho d\tau, \\ R(\rho, \tau) &= \int_{-\infty}^{\infty} \int_{-\infty}^{\infty} \Psi(\kappa, \omega) e^{i(\kappa\rho - \omega\tau)} d\kappa d\omega. \end{aligned}$$

The wavenumber spectrum  $\Theta(\kappa)$  and the frequency spectrum  $\Phi(\omega)$  are both related to  $\Psi$  via

$$\Theta(\kappa) = \int_{-\infty}^{\infty} \Psi(\kappa, \omega) d\omega, \quad \Phi(\omega) = \int_{-\infty}^{\infty} \Psi(\kappa, \omega) d\kappa, \quad (3.2)$$

whence the mean-square of  $u$  fluctuations can be recovered from

$$\langle u'^2 \rangle = \int_{-\infty}^{\infty} \int_{-\infty}^{\infty} \Psi(\kappa, \omega) d\kappa d\omega = \int_{-\infty}^{\infty} \Phi(\omega) d\omega = \int_{-\infty}^{\infty} \Theta(\kappa) d\kappa.$$

These are even,  $\Phi(\omega) = \Phi(-\omega)$  and  $\Theta(\kappa) = \Theta(-\kappa)$ . Since  $\Phi(\omega)$  can be measured directly using hot wires, the one-dimensional longitudinal spectrum,

$$\Theta(\kappa) \equiv \omega'(\kappa)\Phi(\omega(\kappa)), \quad (3.3)$$

strictly defined in terms of a dispersion relation  $\omega(\kappa)$  and associated group velocity  $\omega'(\kappa) \equiv d\omega/d\kappa$ , is often approximated using Taylor's frozen-turbulence hypothesis. Under this assumption, the dispersion relation can be formally written as  $\omega_T(\kappa) = U\kappa$  and, from (3.3),  $\Theta(\kappa) = U\Phi(U\kappa)$ . This is another interpretation to Taylor's hypothesis based on the Fourier decomposition: the group velocity  $\omega'_T(\kappa) = U$  and phase velocity  $\omega_T/\kappa = U$  of all eddies contributing to the turbulent kinetic energy at a particular wall-normal location are constants independent of wavenumber and equal to the mean velocity at that location, an approximation accurate for sufficiently small eddies. To obtain  $\Theta$  from  $\Phi$ , this strict interpretation of Taylor's hypothesis can be relaxed to account for energetic eddies which travel at  $U \pm \Delta U$  provided  $\Psi(\kappa, \omega)$  is symmetric with respect to the  $\omega = U\kappa$  line, that is

$$\Psi(\kappa, \omega) = \Psi(\omega/U, U\kappa), \quad (3.4)$$

because (3.4) then relates the two definitions in (3.2):

$$\Theta(\kappa) \equiv \int_{-\infty}^{\infty} \Psi(\kappa, \omega) d\omega = \int_{-\infty}^{\infty} \Psi(\omega/U, U\kappa) d\omega = U \int_{-\infty}^{\infty} \Psi(\kappa', U\kappa) d\kappa' \equiv U\Phi(U\kappa).$$

For the purpose of obtaining wavenumber spectrum from frequency spectrum, a test of the validity of Taylor's hypothesis can be recast as a question of the symmetry of  $\Psi(\kappa, \omega)$  with respect to the line  $\omega = U\kappa$ . When this symmetry is broken, a different dispersion relation  $\omega_c(\kappa)$  is necessary to relate  $\Phi$  to  $\Theta$ . Since we have access to both  $\Phi$  and  $\Theta$ , we compute the  $\omega_c(\kappa)$  directly by finding the inverse to the monotonic function  $K_t$

$$\omega_c(\kappa) = K_t^{-1}(K_x(\kappa)), \quad K_x(\kappa) \equiv \int_{\kappa}^{\infty} \Theta(\kappa') d\kappa', \quad K_t(\omega) \equiv \int_{\omega}^{\infty} \Phi(\omega') d\omega',$$

where  $K_x(0) = K_t(0) = \langle u'^2 \rangle / 2$ . The analogy to the convection velocity of individual eddies is complex. To first order,  $\omega_c(\kappa)$  describes the apparent passing frequency of the most energetic eddies with wavenumber  $\kappa$ , although this is an integral effect over the range of energetic spanwise wavenumbers.

When computing  $\Psi$  from the present LES simulation, a normalised Hann window in time,  $\sqrt{2/3}[1 - \cos(2\pi n_t/M_t)]$  ( $M_t \Delta_t$  is the temporal window size), is applied to  $\bar{u}$  before taking the discrete Fourier transform because the velocity is not periodic in time. From run G1b (table 1) where  $N_t = 22000$  and  $M_t = 576$ , the spectrum is averaged across  $[22000/(576/2) - 1] = 75$  half-overlapping windows. No windowing is necessary in the periodic streamwise direction.

We plot in figure 2 contours of the premultiplied spectrum,  $\kappa_x \kappa_t \Psi / u_\tau^2$  versus  $\log \lambda_x$  and  $\log \lambda_t$ , where  $\lambda_x = 2\pi/\kappa_x$ ,  $\lambda_t = 2\pi/\kappa_t$  and  $\kappa_t = \omega/U$ . When Taylor's hypothesis is valid, contours of  $\kappa_x \kappa_t \Psi / u_\tau^2$  should be symmetrical about the  $\lambda_t = \lambda_x$  line. Observe from figure 2 that Taylor's hypothesis is indeed a good approximation, except near the wall,  $z/\delta = 0.041$  and  $0.083$ , and for the large scales,  $\lambda_t/\delta, \lambda_x/\delta > 10$ . Note that the LES formulation does not permit effective examination of smaller scales or locations closer to the wall. The dispersion relation line computed from  $\Psi$ ,  $\lambda_t = \lambda_x \omega / \omega_c$ , appearing below

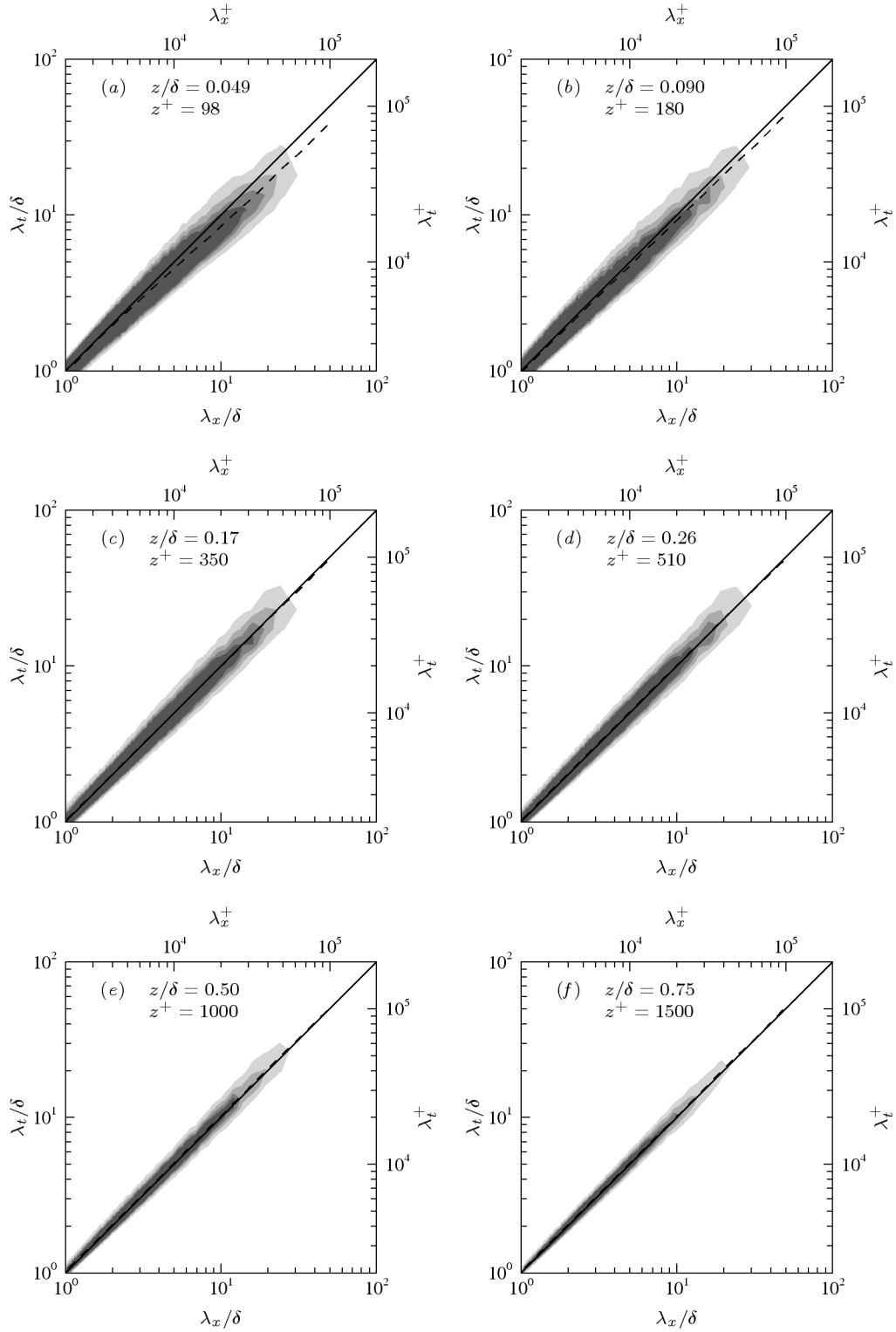


FIGURE 2. Premultiplied spatio-temporal spectra of streamwise velocity fluctuations,  $\kappa_x \kappa_t \Psi / u_\tau^2 = 0.1, 0.2, 0.3, 0.4$ , at various heights from  $Re_\tau = 2k$  channel flow LES, run G1b (table 1):  $---$ , dispersion relation computed from  $\Psi$ ,  $\lambda_t = \lambda_x \omega / \omega_c$ ;  $—$ , Taylor's hypothesis  $\lambda_t = \lambda_x$ .

(to the right) of Taylor’s hypothesis,  $\lambda_t = \lambda_x \omega / \omega_T = \lambda_x \cdot 1$ , implies that the phase velocity  $U_c \equiv \omega_c / \kappa$  is larger than the mean velocity  $U$ .

Despite overwhelming similarities, the phase velocity  $U_c$  is not strictly the same as the convection velocity defined by (2.7) from Wills (1964), where it is related to the ridge of  $\Psi$ . Recall from (3.3) that by construction  $U_c(\kappa)$  is defined such that the wavenumber spectrum  $\Theta$  can be recovered from the frequency spectrum  $\Phi$ , that is  $\Theta(\kappa) \equiv \Phi(\kappa U_c(\kappa)) d(\kappa U_c(\kappa)) / d\kappa$ . Put another way, it is the mapping from wavenumber space to frequency space such that the energy observed in wavenumber space at the wavenumber  $\kappa$ ,  $\Theta(\kappa) d\kappa$ , is equal to that observed in frequency space  $\Phi(\kappa U_c(\kappa)) d(\kappa U_c(\kappa))$  at frequency  $\omega = \kappa U_c(\kappa)$  (see also discussion in Monty & Chong (2009)). In practice, see figure 2, this integral-based definition often traces out the ridge of  $\Psi$ , that is the definition in Wills (1964). Because it can be measured readily, the ridge-based definition is often taken as the surrogate for  $U_c$ . Energy transmission occurs at neither  $U_c$  nor the velocity given by Wills (1964), but the group velocity  $d(\kappa U_c(\kappa)) / d\kappa$ , that is the velocity of the energy of wavepackets with wavenumber near  $\kappa$ . Summarising, to obtain the wavenumber spectrum from the frequency spectrum, we require both the phase velocity and group velocity, see (3.3): the former appearing in the argument of  $\Phi$  as  $\kappa U_c(\kappa)$  to rescale the frequency; and the latter appearing as a factor of  $\Phi$  as  $d(\kappa U_c(\kappa)) / d\kappa$  to rescale the rate of change in frequency.

Following Dennis & Nickels (2008), we can also test the validity of Taylor’s hypothesis in physical space by plotting the autocorrelation  $R$  defined by (3.1). Taylor’s hypothesis is valid, or more precisely there is a straightforward conversion from the temporal to the spatial domain, where the contours of  $R$  are symmetrical about the  $\rho_x = \rho_t$  line, where  $\rho_t = \tau U$ . Like figure 2,  $R$  in figure 3 shows an unequivocal departure from Taylor’s hypothesis near the wall,  $z/\delta = 0.041$  and  $0.083$  and for the large scales,  $\rho_t/\delta, \rho_x/\delta > 10$ . There also appears to be a slight discrepancy of the opposite sign for the large scales at  $z/\delta = 0.5$ , which is more marked in the autocorrelation than our presentation of the spectrum. The boundary layer PIV experiment performed by Dennis & Nickels (2008) at  $Re_\theta \approx 4.7$  k reported that Taylor’s hypothesis is still valid at the height  $z/\delta = 0.16$  for the field of view  $\rho/\delta < 0.29$  m/0.09 m = 3.2 and  $\tau U/\delta < 1$  s  $\times$  0.57 ms<sup>-1</sup>/0.09 m = 6.3. This is consistent with the present LES data since at  $z/\delta = 0.17$ , figure 3(c),  $R$  is indeed symmetrical about the  $\rho_x = \rho_t$  line, even up to very large scales  $\rho_t, \rho_x = 20\delta$ .

Consideration of spatio-temporal spectra permits some speculation about the convection velocities of the energetic structures and the error associated with identifying the footprint of eddies with a particular streamwise scale on the near-wall region from temporal data. The LES velocity fields unequivocally indicate that the most energetic large structures convect faster than the local mean velocity close to the wall, with the deviation growing close to the wall. Conversely, these large structures convect slower than the local mean velocity near the channel centre, figure 3(e, f). This suggests that these eddies are “local” to a region in the overlap layer, in the sense that the mean velocity matches their convective velocity somewhere in the log region. We speculate that the location of this velocity matching corresponds to the location of the large-scale streamwise energy peak, which is consistent with the approximate magnitude of the difference between  $\omega/\omega_T$  and  $\omega/\omega_c$  for large wavelength. This suggests that the departure from Taylor’s hypothesis at the large scales should strengthen with increasing Reynolds number due to the increasing shear near the wall. This is an area of current experimental study.

### 3.2. Large-scale–small-scale interaction

With the differences between the spatial and the temporal decompositions in mind, we now describe the correlation that characterizes the interaction between the large-scales



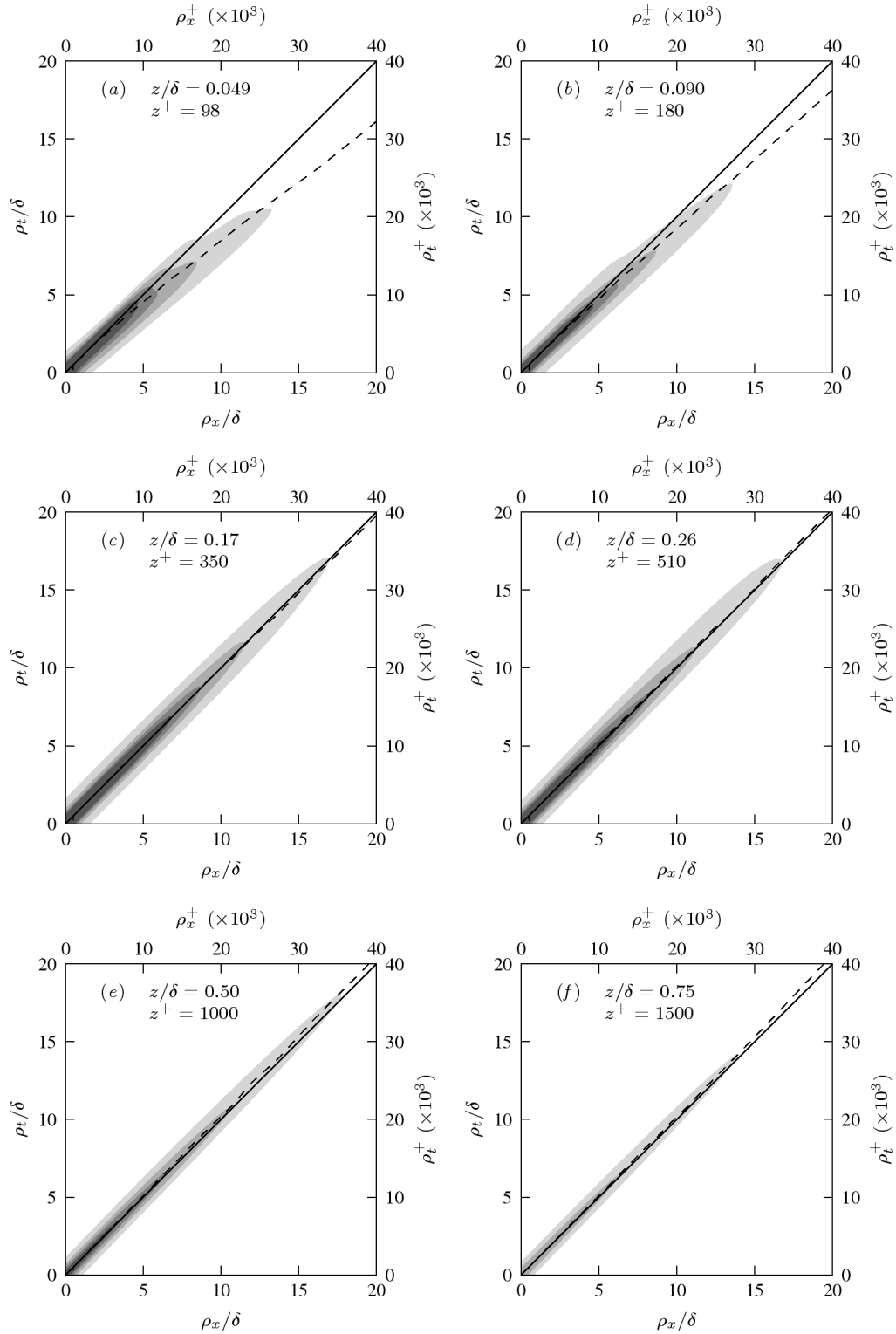


FIGURE 3. Spatio-temporal correlations of streamwise velocity fluctuations,  $R/u_\tau^2 = 0.3, 0.6, 0.9, 1.2$ , at various heights from  $Re_\tau = 2k$  channel flow LES, run G1b (table 1):  $---$ , dispersion relation computed from  $\Psi$ ,  $\rho_t = \rho_x \omega / \omega_c$ ;  $—$ , Taylor's hypothesis  $\rho_t = \rho_x$ .



and the small-scales. We first extract the large-scale fluctuations  $u_L$  by applying a sliding-window top-hat time average, centred at  $t$ , to  $u$ :

$$u_L(t) = \frac{1}{\tau} \int_{t-\tau/2}^{t+\tau/2} u(t') dt', \quad (3.5)$$

where  $\tau$  is the width of the sliding window. A low-pass filter, (3.5), dampens fluctuations with frequencies higher than  $1/\tau$ . In spectral space, (3.5) is equivalent to a multiplication by the filter  $\sin(\tau\omega/2)/(\omega/2)$ , where  $\omega$  is the angular frequency. For clarity, we have suppressed the  $\mathbf{x}$ -dependence of  $u$  in this part of the discussion since  $\mathbf{x}$  is held constant.

The small-scale fluctuations are defined to be the remaining part of the motion,  $u_S = u - u_L$ . The small-scale intensity can be measured by its local r.m.s.,

$$\tilde{u}_S(t) = \left( \frac{1}{\tau} \int_{t-\tau/2}^{t+\tau/2} u_S^2(t') dt' \right)^{1/2}. \quad (3.6)$$

Physically,  $\tilde{u}_S$  measures the local envelope or intensity of small-scale fluctuations. For example, if  $u_S$  is normally distributed, 95% of its amplitude is estimated to lie within  $2\tilde{u}_S$ . If  $u_S$  is not normal,  $\tilde{u}_S$  still measures the spread or envelope of  $u_S$ . In any case,  $\tilde{u}_S^2$  appears in the equations governing  $u_L$ , obtained by applying the filter (3.5) to the Navier–Stokes equations (see Reynolds & Hussain (1972) for a related two-scale decomposition), which is another way to interpret  $\tilde{u}_S$ . Note that equivalent approaches have been used by Bandyopadhyay & Hussain (1984) and Guala, Metzger & McKeon (2009) to obtain similar results in a range of flows including a laboratory turbulent boundary layer and the near-wall region of the near neutrally stable atmospheric surface layer, respectively.

An elegant alternative to obtain the envelope of  $u_S$  is via the Hilbert transform (Mathis *et al.* 2009), and this approach has led to a significant advance in understanding of the large-small scale interactions. However it is harder to relate the results to the governing equations of turbulence.

When calculating an r.m.s. defined locally, (3.6), one has to contend with the inevitability that large-scales (low frequencies) have been aliased into the small-scale signature. Perhaps a better alternative is to use a tapered window in (3.6), alleviating some but not all of the aliasing. We have tried this and found some minor changes, but the general picture is unaltered, and so we decided to keep the simple definition in (3.6). The Hilbert transform bypasses this aliasing difficulty at the enveloping stage, but the issue reappears when one filters the envelope signal. We note that even if a perfect decomposition can be found, nature herself does not permit it, that is the two peaks in  $\kappa_x E_{uu}$  (Hutchins & Marusic 2007b) are never completely isolated, at least in Fourier space.

In terms of LES quantities, we can write (3.5) and (3.6) as

$$u_L(t) = \frac{1}{\tau} \int_{t-\tau/2}^{t+\tau/2} \bar{u}(t') dt', \quad (3.7a)$$

$$\tilde{u}_S(t) = \left( \frac{1}{\tau} \int_{t-\tau/2}^{t+\tau/2} [u_S^2(t') + T_{xx}(t')] dt' \right)^{1/2}, \quad (3.7b)$$

where  $\bar{u}$  is the resolved velocity;  $u_S = \bar{u} - u_L$ ; and  $T_{xx}$  is the modelled subgrid fluctuations associated with time scales smaller than the numerical discretization  $\Delta_t$ . Using (3.7), we now construct the normalised large-scale–small-scale correlation based on temporal

filtering:

$$R_\tau(z) = \frac{\langle (u_L - U)(\tilde{u}_S - \langle \tilde{u}_S \rangle) \rangle}{\langle (u_L - U)^2 \rangle^{1/2} \langle (\tilde{u}_S - \langle \tilde{u}_S \rangle)^2 \rangle^{1/2}}, \quad (3.8)$$

where the global or ensemble average is formally given by

$$\langle \phi \rangle \equiv \lim_{T \rightarrow \infty} \frac{1}{T} \int_{-T/2}^{T/2} \phi(t') dt'. \quad (3.9)$$

Note that the visual envelope of  $u_S$ , e.g.  $2\tilde{u}_S$ , does not affect  $R_\tau$  because the constant factor cancels out in the normalised correlation (3.8). In other words,  $R_\tau$  does not contain amplitude information; it does, however, contain phase information, since it is the cosine of the angle (or phase) between  $u_L - U$  and  $\tilde{u}_S - \langle \tilde{u}_S \rangle$ , using the inner product  $\langle \cdot \rangle$ . In practice, we obtain  $R_\tau(z)$  by replacing the integrals with sums and ensuring the recording period  $T$  is much larger than the largest physical time scale in the flow, see table 1.

The spatial counterpart to (3.8),  $R_\rho(z)$ , is defined analogously, with  $x$  and  $\rho$  respectively replacing  $t$  and  $\tau$ , while holding other variables constant. For  $R_\rho$ , the global average (3.9) is replaced by an average over the wall-parallel plane with area  $L_x L_y$ . The spatial correlations are calculated from runs G1 and H3 at one snapshot in time.

The physical meaning of the correlations  $R = R_\tau, R_\rho$  are as follows. If large-scale higher-speed regions carry higher small-scale intensity (positively correlated, in phase), then  $R \approx 1$ . Similarly, if large-scale higher-speed regions carry lower small-scale intensity (negatively correlated,  $\pi$  out of phase), then  $R \approx -1$ .  $R \approx 0$  can occur either if there is no correlation between the large and small scales, or if they are  $\pi/2$  out of phase, which is physically the more likely option given the strong correlation for small and large  $z/\delta$ , as already demonstrated by Bandyopadhyay & Hussain (1984); Mathis *et al.* (2009).

Although the r.m.s.-based correlation coefficient (3.8) is different from its Hilbert-transform-based counterpart in the boundary layer study of Mathis *et al.* (2009), we expect similar qualitative features if the large-scale–small-scale phase relationship is a universal aspect of wall-bounded flows, namely channels and boundary layers. As we are interested in large scales with sizes of the order  $10\delta$ , we expect that the LES will capture this statistic satisfactorily since the premise of an LES is to directly simulate the large scales; presently, there are 6 grid points per  $\delta$  in both wall-parallel directions and 24 grid points per  $\delta$  in the wall-normal direction.

Figure 4 compares the correlations based on temporal filtering,  $R_\tau$ , and correlations based on spatial filtering,  $R_\rho$ , for  $Re_\tau = 2\text{ k}$  and  $Re_\tau = 200\text{ k}$  and different values of  $\tau$  and  $\rho$ . Observe that near the wall,  $u_L$  and  $\tilde{u}_S$  are positively correlated, up to  $R \approx 0.4$  (the maximum in the domain we resolve, although note that the maximum value likely increases closer to the wall), but above a certain crossing height,  $z/\delta \approx 0.2$  for  $Re_\tau = 2\text{ k}$  and  $z/\delta \approx 0.11$  for  $Re_\tau = 200\text{ k}$ , they are negatively correlated, down to  $R \approx -0.4$ . The trend of decreasing crossing height with increasing Reynolds number is also reported by Mathis *et al.* (2009) for the turbulent boundary layer, with  $z/\delta \approx 0.07$  for  $Re_\tau = 2.8\text{ k}$  and  $z/\delta \approx 0.03$  for  $Re_\tau = 19\text{ k}$ . Presently, the correlations are largely independent of filter sizes  $1.7 < \tau U/\delta, \rho/\delta < 12.3$ , although the deviation between  $R_\rho$  and  $R_\tau$  with the larger filter sizes from the one with  $\rho/\delta = 1.7$  close to the wall is exacerbated in the spatial plots, as would be expected from the arguments concerning Taylor’s hypothesis at the large scales in the preceding section. The kick-up of  $R_\rho$  relative to  $R_\tau$  for curves corresponding to  $\rho/\delta = 7.0, 12.3$  in the vicinity of  $z/\delta = 0.45$ , see figure 4(a, b) is presumably related to the convection velocity effect demonstrated in figure 3(e). A small sensitivity to filter sizes is reported by Mathis *et al.* (2009). Perhaps a precise quantitative comparison is impossible owing to the different envelope-extraction techniques and the different type

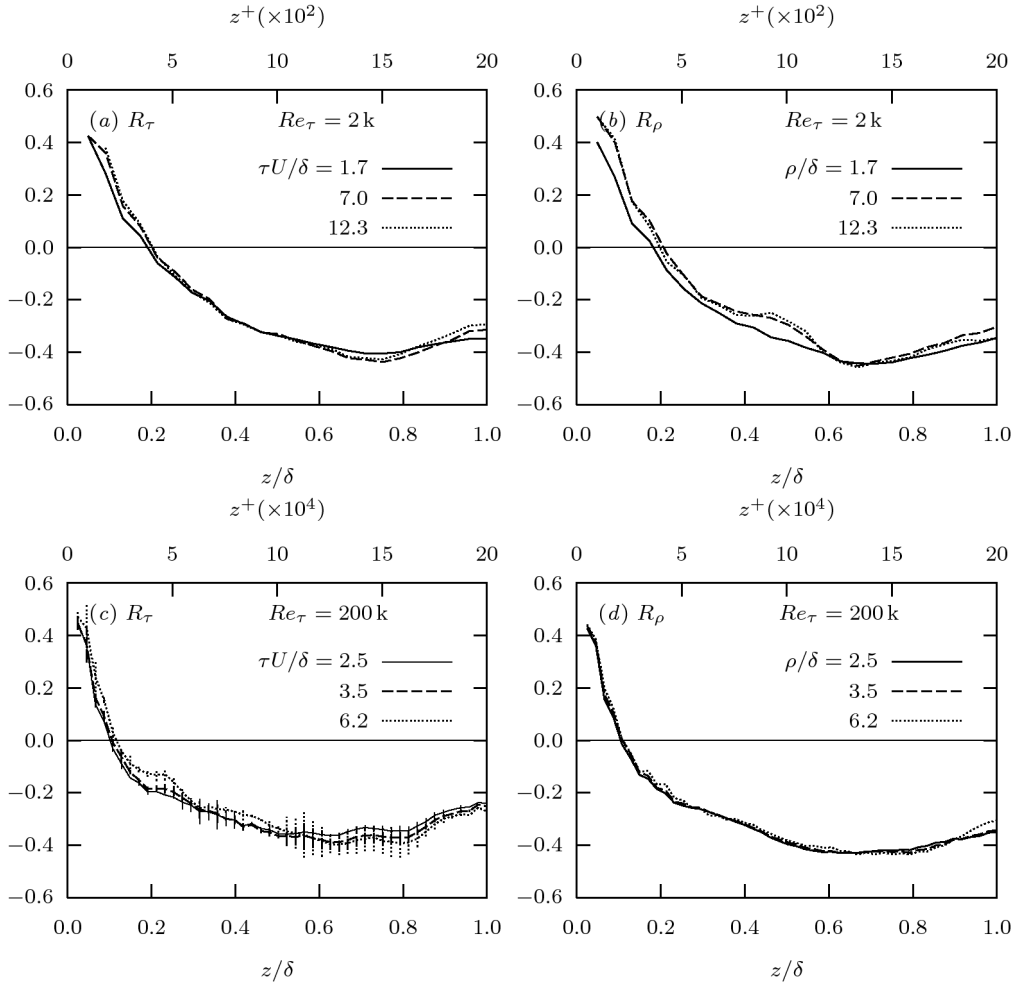


FIGURE 4. Profiles of large-scale–small-scale correlations,  $R_\tau$  and  $R_\rho$ , defined by (3.8). Filter sizes and  $Re_\tau$  inset. Error lines in (c) indicate convergence uncertainties from inadequate averaging period  $T$ . Data from channel flow LES, runs G1 and H3 (table 1).

of wall-bounded flows. Note that a robust feature is that  $R$  increases slightly at the centre of the channel, but remains negative (figure 4). This increase is also reported in Mathis *et al.* (2009) (and this sensitivity appears to be slightly enhanced in the case of the spatial correlation), but their increase is from negative correlations to positive correlations, a feature possibly related to the intermittent boundary layer thickness not present in channel flows.

Although the large-scale–small-scale interaction was recently (Mathis *et al.* 2009) framed in terms of amplitude modulation, the results could also be discussed in terms of the relative phase between the large and small scales, as originally posed by Bandyopadhyay & Hussain (1984) and implied by the formulation of (3.8).

### 3.3. Conditionally averaged large-scale velocities and small-scale intensities

To gain some insight into the structure of the large-scale coherent regions and the phase relationship between  $u_L$  and  $\tilde{u}_S$  shown in figure 4, we now turn our attention to conditionally averaged  $u_L$  and  $\tilde{u}_S$  fields computed with the streamwise filter window  $\rho = \delta$ . As

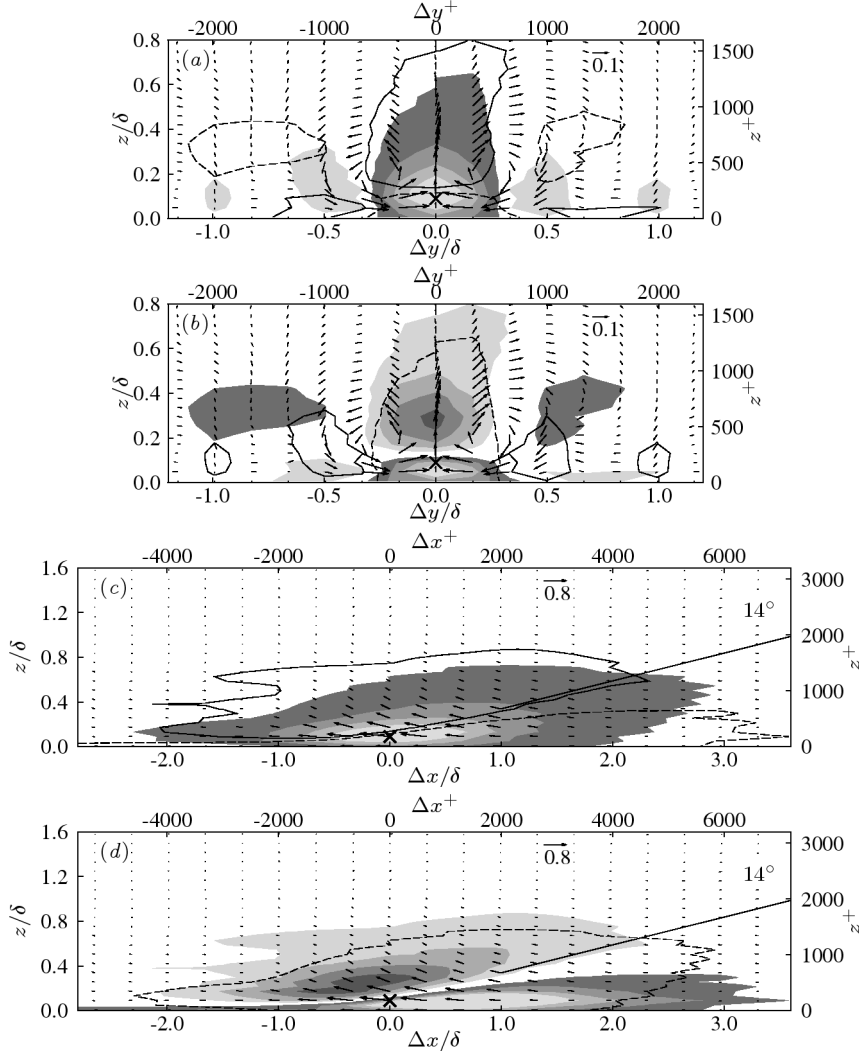


FIGURE 5. Conditionally averaged streamwise velocity fields in the (a, b) spanwise-wall-normal and (c, d) streamwise-wall-normal planes, with  $\langle u_L^+ | A_1 \rangle(\Delta \mathbf{x})$  and  $\langle \tilde{u}_S^+ | A_1 \rangle(\Delta \mathbf{x})$ , where  $A_1$  is the low-speed event  $u_L(\mathbf{x}_\times) - U < 0$  with probability  $P\{A_1\} = 0.53$  at  $\mathbf{x}_\times/\delta = (0, 0, 0.090)$ : (a, c) filled contours of  $|\langle u_L^+ | A_1 \rangle - U^+| = 0.1, 0.3, 0.5, 0.7$ , line contours of  $|\langle \tilde{u}_S^+ | A_1 \rangle - \langle \tilde{u}_S^+ \rangle| = 0.01$ ; and (b, d) filled contours of  $|\langle \tilde{u}_S^+ | A_1 \rangle - \langle \tilde{u}_S^+ \rangle| = 0.01, 0.02, 0.03, 0.04$ , line contours of  $|\langle u_L^+ | A_1 \rangle - U^+| = 0.1$ . Darker to lighter shades and dashed lines for negative values. Vectors represent in-plane velocity components. Data from snapshot of  $Re_\tau = 2$  k channel flow LES, run G1b (table 1).

seen in figure 4 and in Mathis *et al.* (2009), this phase relationship is relatively unaffected by the choice of  $\rho$ .

Figure 5 shows ensemble averages,  $\langle u_L | A_1 \rangle(\Delta \mathbf{x})$  and  $\langle \tilde{u}_S | A_1 \rangle(\Delta \mathbf{x})$ , conditioned on the occurrence of a large-scale low-speed event at  $z/\delta = 0.090$ ,  $A_1 = u_L(\mathbf{x}_\times) - U < 0$ , where  $\Delta \mathbf{x} = \mathbf{x} - \mathbf{x}_\times$ ,  $\mathbf{x}_\times^+ = (0, 0, 180) \Leftrightarrow \mathbf{x}_\times/\delta = (0, 0, 0.090)$ , computed from a snapshot of LES run G1b (table 1). The spanwise-wall-normal view, figure 5(a), is previously shown in figure 7(a) of Hutchins & Marusic (2007b) with the choice  $z_\times^+ = 150$  from the DNS data of del Álamo *et al.* (2004) at  $Re_\tau \approx 1$  k. For reference, the vectors in figure

5(a, b) correspond to LES discretization points. The agreement between DNS and LES results is striking. The essential features of the DNS averages are also seen in the present LES averages, namely 1) a splatted low-speed region with minimum  $\langle u_L^+ | A_1 \rangle \approx -0.8$  and width  $\Delta y / \delta \approx 0.4$  centred on  $\mathbf{x}_\times$  flanked on both sides by weaker high-speed regions with maximum  $u_L^+ \approx 0.1$ ; and 2) the in-plane large-scale swirl at  $\Delta_x / \delta \approx \pm 0.2$ ,  $z / \delta \approx 0.2$ .

We report that  $P\{A_1\} = 0.53$ , implying that nearly identical figures, but with signs reversed, are seen when we condition on the large-scale high-speed event  $A'_1 = u_{L\times} - U > 0$  (the complement of  $A_1$ ) because

$$0 = \langle \phi \rangle \equiv \langle \phi | A_1 \rangle P\{A_1\} + \langle \phi | A'_1 \rangle P\{A'_1\} \quad \Rightarrow \quad \langle \phi | A_1 \rangle \approx -\langle \phi | A'_1 \rangle,$$

(equality holds if  $P\{A_1\}$  is exactly 1/2). Since the reversed picture, conditioned on  $A'_1$  exists, neighbouring high-speed regions in figure 5(a) could be interpreted as equal-magnitude high-speed regions whose strengths have been smeared by other less-dominant large-scale dispersive motions in the averaging process. Thus, a detailed description of physical processes far away from  $\mathbf{x}_\times$  is difficult to ascertain. One may be tempted to believe from the conditional average fields that these structures are aligned in the streamwise direction; instantaneous visualisations, see Monty *et al.* (2007), suggest that these are in fact meandering structures, which would have been obscured in the averaging over the periodic domain in our study. However this apparent meandering coherence could equally well be interpreted as adjoined regions of shorter coherence, which are individually well-captured by the conditional averaging. The spanwise scale appears to be approximately  $\delta$ .

Figure 5(b) shows the spanwise structure of the relationship between  $u_L$  and  $\tilde{u}_S$ : near the wall,  $u_L$  and  $\tilde{u}_S$  are positively correlated, but above  $z / \delta \approx 0.1$ , they are negatively correlated. This crossing point is different from  $z / \delta \approx 0.2$  seen in figure 4(a). The discrepancy is resolved by noting the inclusive ( $A_1 = u_L - U > 0$ ) and non-collocated (two-point) nature of the conditioning used for the averages  $\langle u_L | A_1 \rangle$  and  $\langle \tilde{u}_S | A_1 \rangle$ , as well as the single plane rather than integral representation. In contrast, the correlation  $R$ , see (3.8), is constructed from the one-point collocated statistic,  $\langle u_L \tilde{u}_S \rangle \equiv \int \langle u_L | u_L \rangle \langle \tilde{u}_S | u_L \rangle p(u_L) du_L$ , which is not the same as  $\sum_A \langle u_L | A \rangle \langle \tilde{u}_S | A \rangle P\{A\}$ . The opposite  $u_L - \tilde{u}_S$  configuration of the weaker flanking regions in figure 5(b) suggests that these too experience phase reversal.

Figure 5(c, d) shows the streamwise-wall-normal structure of the dominant large-scale motion and the relationship between the small and large scales. Despite a filter size of  $\delta$ , the coherence indicated in the figure suggests a wavelength of order  $6\delta$ , suggesting that the very long structures are the dominant contributors to the  $u_L(\mathbf{x}_\times) - U < 0$  signal. Clearly the large-scale coherence has a streamwise phase that is dependent on the wall-normal location, at least where the coherence is strongest. Close to the wall this phase variation is weak, while the conditional averages with  $\mathbf{x}_\times^+ = (0, 0, 1000) \Leftrightarrow \mathbf{x}_\times / \delta = (0, 0, 0.5)$  shown in figure 6 show that far from the wall the phase variation with increasing  $z / \delta$  is also weak, but close to  $\pi$  rather than zero. In the intermediate region, the phase changes rapidly with wall-normal distance. The contours of constant  $|\tilde{u}_S^+ - \langle \tilde{u}_S^+ \rangle|$  in figure 5(d) reveal a surface that cuts through the large-scale, low-speed region at a diagonal such that the region of negative correlation is larger where  $\Delta x < 0$  but smaller where  $\Delta x > 0$ . The angle of this separatrix, at least in the aforementioned intermediate region, is about  $14^\circ$ , suggesting that the modulation reversal (Mathis *et al.* 2009) is related to the structure inclination angle (Marusic & Heuer 2007).

Figure 5(c, d) and  $P\{A_1\} \approx 1/2$  suggest the stylised picture of a streamwise train of alternating high-speed and low-speed regions with the shape in figure 5(c). We propose that this sign change of  $u_L - U$  determines the shape of the  $\tilde{u}_S$  region over a range

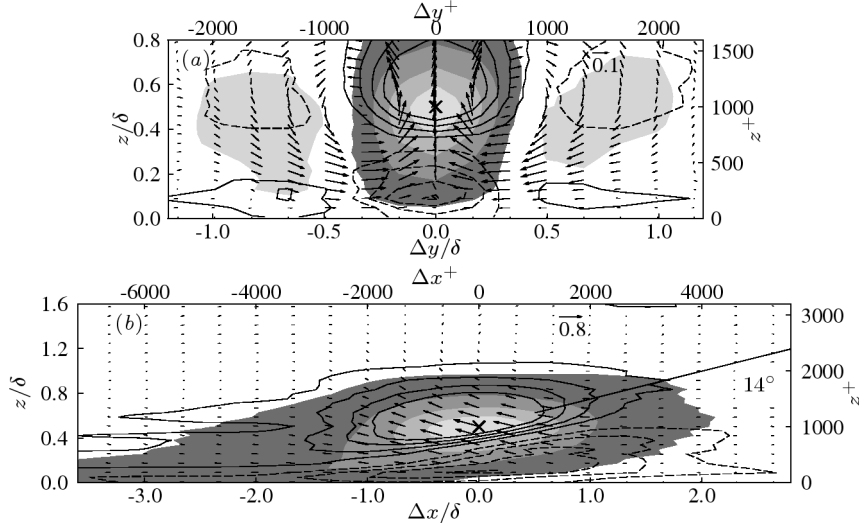


FIGURE 6. Conditionally averaged streamwise velocity fields in the (a) spanwise–wall-normal and (b) streamwise–wall-normal planes, with  $\langle \mathbf{u}_L^+ | A_2 \rangle(\Delta \mathbf{x})$  and  $\langle \tilde{u}_S^+ | A_2 \rangle(\Delta \mathbf{x})$ , where  $A_2$  is the low-speed event  $u_L(\mathbf{x}_\times) - U < 0$  with probability  $P\{A_2\} = 0.47$  at  $\mathbf{x}_\times/\delta = (0, 0, 0.5)$ : filled contours of  $|\langle u_L^+ | A_2 \rangle - U^+| = 0.1, 0.3, 0.5, 0.7$ , line contours of  $|\langle \tilde{u}_S^+ | A_2 \rangle - \langle \tilde{u}_S^+ \rangle| = 0.01, 0.02, 0.03, 0.04$ . Darker to lighter shades and dashed lines for negative values. Vectors represent in-plane velocity components. Data from snapshot of  $Re_\tau = 2k$  channel flow LES, run G1b (table 1).

of wall-normal distances. Consider the governing equation for  $\tilde{u}_S^2$ , which contains the production term  $-2\tilde{u}_S^2 \partial u_L / \partial x$  (Reynolds & Hussain 1972). Now,  $\partial u_L / \partial x < 0$  in between a high-speed region placed upstream ( $-\Delta x$ ) of a low-speed region. Then, the production  $-2\tilde{u}_S^2 \partial u_L / \partial x > 0$  increases  $\tilde{u}_S^2$ , resulting in the picture 5(d). The opposite mechanism applies in between a low-speed region placed upstream of a high-speed region, in which case  $-2\tilde{u}_S^2 \partial u_L / \partial x < 0$ , a backscatter of small-scale streamwise energy. This results in the quarter-phase shift between the  $u_L$  and  $\tilde{u}_S$  region.

A clearer picture emerges when we compute averages conditioned on the  $u_L > 0$  to  $u_L < 0$  boundary, signalled by the event  $A_3 = (\partial u_L / \partial x)(\mathbf{x}_\times) < 0$  (figure 7), interpreted as a quarter-phase streamwise shift of figure 5(c, d). As expected,  $\tilde{u}_S$  is lowest precisely where  $\partial u_L / \partial x$  is minimum (at  $\mathbf{x}_\times$ ), figure 7(b). The bulge-like shape of the  $u_L$  regions is preserved, see figure 7(a), although with smaller sizes. Like the average conditioned on  $A_1$ , this figure is also reversible, with  $P\{A_3\} = 0.48$ .

The interactions further from the wall can be investigated by repeating the conditional averaging at  $\mathbf{x}_\times/\delta = (0, 0, 0.5)$ . A different relationship between the large and small scale activity emerges, as shown in figure 6. Instead of the  $0-\pi/2$  phase difference close to the wall,  $|u_L^+ - U^+|$  and  $|\tilde{u}_S^+ - \langle \tilde{u}_S^+ \rangle|$  are substantially out of phase, that is the phase difference is approximately  $\pi$ . This variation is in good agreement with boundary layer results over a Reynolds number range of three decades, namely Bandyopadhyay & Hussain (1984) and the recent work of Guala *et al.* (2009). From these other works, it would be expected that the large and small scales have close to zero phase difference very close to the wall; the LES formulation prevents us from confirming this point.

A visual inspection of figure 5 gives an estimate that  $\mathbf{u}_L^+$  is of the order  $(0.8, 0.2, 0.05)$ . Thus, the shear stress carried directly by these large-scale structures is estimated from this conditionally averaged picture as  $-\langle u_L w_L \rangle^+ \approx 0.04$ , and the large-scale streamwise

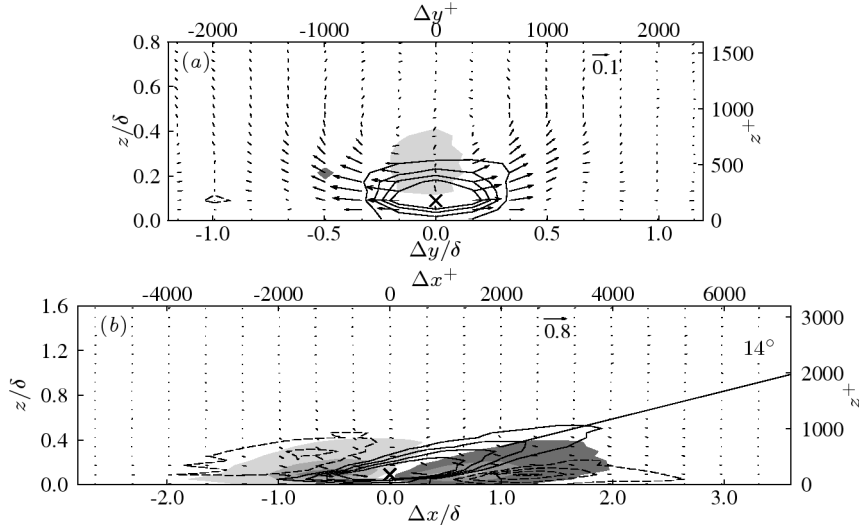


FIGURE 7. Conditionally averaged streamwise velocity fields in the (a) spanwise–wall-normal and (b) streamwise–wall-normal planes, with  $\langle u_L^+ | A_3 \rangle(\Delta \mathbf{x})$  and  $\langle \tilde{u}_S^+ | A_3 \rangle(\Delta \mathbf{x})$ , where  $A_3$  is the streamwise high-speed-to-low-speed boundary event  $(\partial u_L / \partial x)(\mathbf{x}_\times) < 0$  with probability  $P\{A_3\} = 0.48$  at  $\mathbf{x}_\times / \delta = (0, 0, 0.090)$ : filled contours of  $|\langle u_L^+ | A_3 \rangle - U^+| = 0.1, 0.3, 0.5, 0.7$ , line contours of  $|\langle \tilde{u}_S^+ | A_3 \rangle - \langle \tilde{u}_S^+ \rangle| = 0.01, 0.02, 0.03, 0.04$ . Darker to lighter shades and dashed lines for negative values. Vectors represent in-plane velocity components. Data from snapshot of  $Re_\tau = 2k$  channel flow LES, run G1b (table 1).

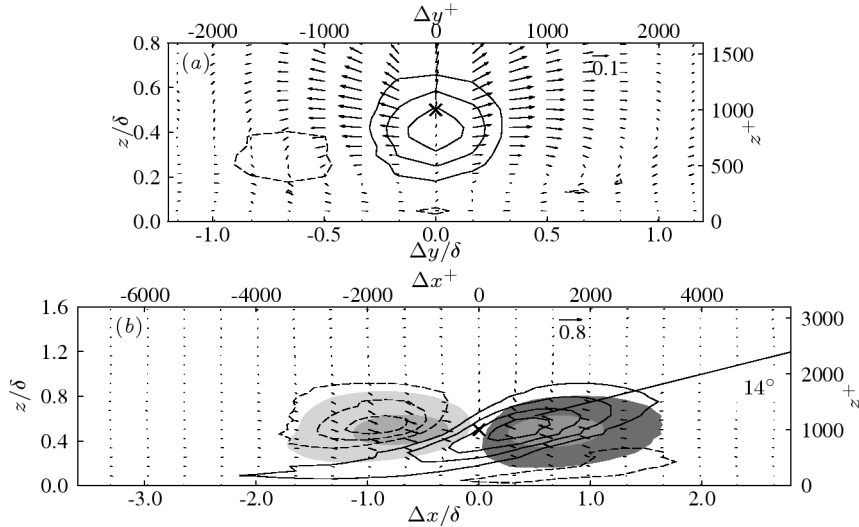


FIGURE 8. Conditionally averaged streamwise velocity fields in the (a) spanwise–wall-normal and (b) streamwise–wall-normal planes, with  $\langle u_L^+ | A_4 \rangle(\Delta \mathbf{x})$  and  $\langle \tilde{u}_S^+ | A_4 \rangle(\Delta \mathbf{x})$ , where  $A_4$  is the streamwise high-speed-to-low-speed boundary event  $(\partial u_L / \partial x)(\mathbf{x}_\times) < 0$  with probability  $P\{A_4\} = 0.48$  at  $\mathbf{x}_\times / \delta = (0, 0, 0.5)$ : filled contours of  $|\langle u_L^+ | A_4 \rangle - U^+| = 0.1, 0.3, 0.5, 0.7$ , line contours of  $|\langle \tilde{u}_S^+ | A_4 \rangle - \langle \tilde{u}_S^+ \rangle| = 0.01, 0.02, 0.03, 0.04$ . Darker to lighter shades and dashed lines for negative values. Vectors represent in-plane velocity components. Data from snapshot of  $Re_\tau = 2k$  channel flow LES, run G1b (table 1).



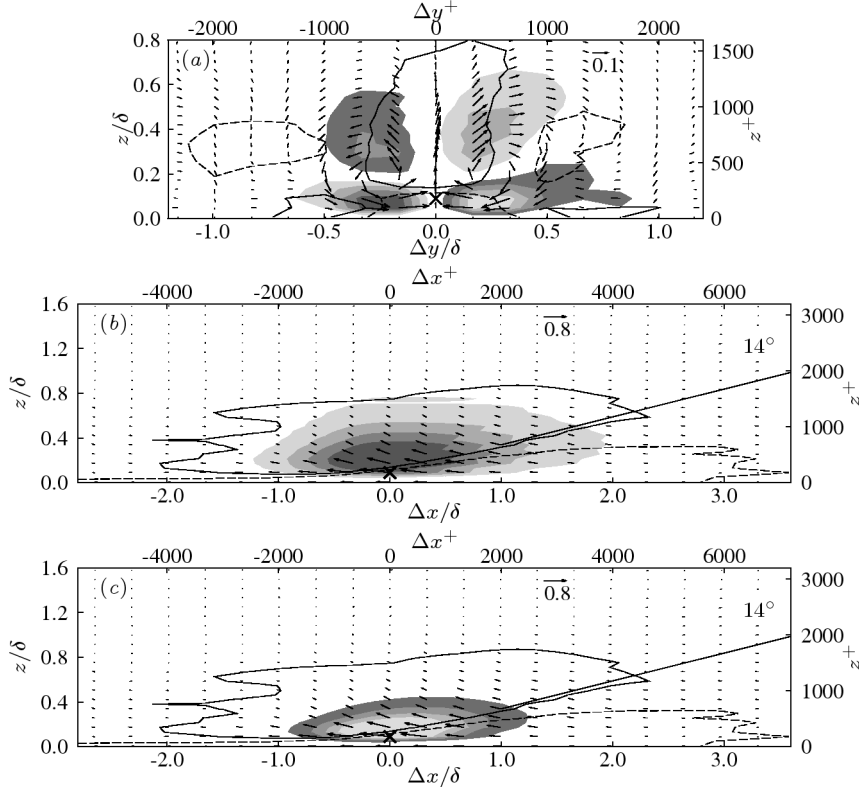


FIGURE 9. Spanwise and wall-normal velocities, and Reynolds stress associated with the conditionally averaged streamwise velocity in the (a) spanwise–wall-normal and (b, c) streamwise–wall-normal planes, with  $\langle \mathbf{u}_L^+ | A_1 \rangle (\Delta \mathbf{x})$  and  $\langle \tilde{u}_S^+ | A_1 \rangle (\Delta \mathbf{x})$ , where  $A_1$  is the low-speed event  $u_L(\mathbf{x}_\times) - U < 0$  with probability  $P\{A_1\} = 0.53$  at  $\mathbf{x}_\times/\delta = (0, 0, 0.090)$ : (a) filled contours of  $|\langle \tilde{v}_L^+ | A_1 \rangle| = 0.04, 0.08, 0.12, 0.16$ ; (b) filled contours of  $|\langle \tilde{w}_L^+ | A_1 \rangle| = 0.03, 0.06, 0.09, 0.12$ ; (c) filled contours of  $|\langle \tilde{w}_L^+ | A_1 \rangle (\langle \tilde{w}_L^+ | A_1 \rangle - U^+)| = 0.02, 0.04, 0.06, 0.08$ ; and (a–c) line contours of  $|\langle \tilde{u}_S^+ | A_1 \rangle - \langle \tilde{u}_S^+ \rangle| = 0.01$ . Darker to lighter shades and dashed lines for negative values. Vectors represent in-plane velocity components. Data from snapshot of  $Re_\tau = 2k$  channel flow LES, run G1b (table 1).

intensity is estimated as  $\langle u_L^2 \rangle^+ \approx 0.64$ . The relative magnitude and phase of the other velocity components associated with the large scale structure can be confirmed by looking at equivalent conditional averages for the other velocity components. Note that it is extremely difficult to obtain this sort of data experimentally, so we are effectively using the LES data in a predictive capacity to complete the description of the trends in the structure of the large-scale motions.

Figures 9–11(a, b) reveal that while the spanwise velocity exhibits a footprint consistent with the implied swirl of figure 5, such that  $v_L = 0$  statistically on the conditioning plane, but with a wall-normal phase variation similar to that exhibited by the streamwise velocity  $u_L$ . By contrast, the wall-normal velocity velocities in figures 9–11(c) are substantially in phase in the wall-normal direction, independent of the conditioning criterion.

The conditional averaging technique can be taken one step further to demonstrate that, despite a large wall-normal footprint in the streamwise velocity, the large scales will contribute locally to the mean shear stress because of the relative wall-normal phases of the

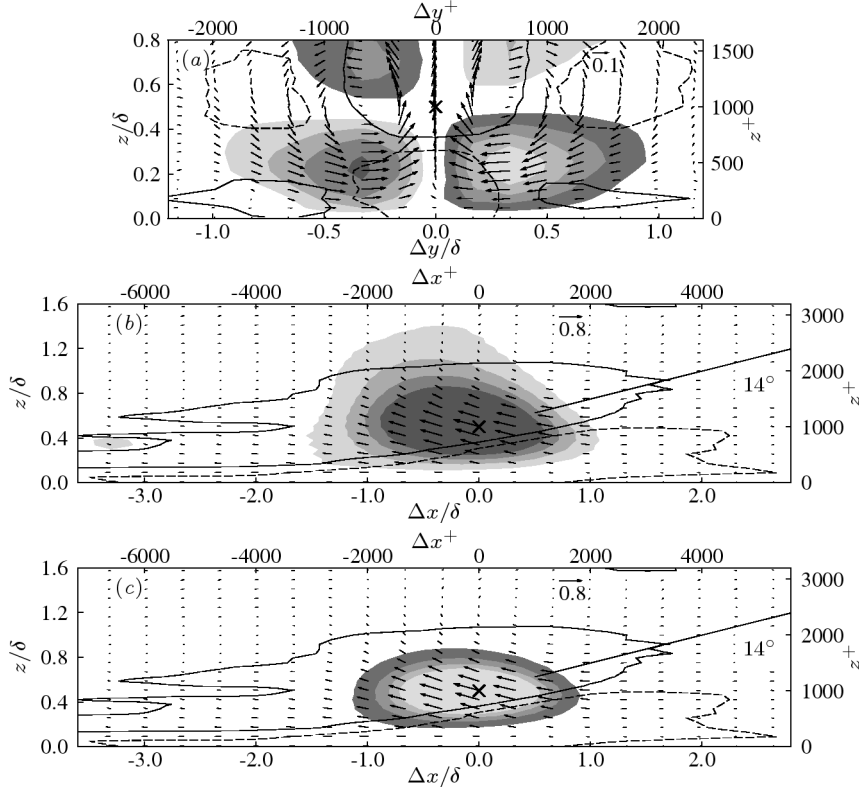


FIGURE 10. Spanwise and wall-normal velocities, and Reynolds stress associated with the conditionally averaged streamwise velocity in the (a) spanwise–wall-normal and (b, c) streamwise–wall-normal planes, with  $\langle \mathbf{u}_L^+ | A_2 \rangle(\Delta \mathbf{x})$  and  $\langle \tilde{u}_S^+ | A_2 \rangle(\Delta \mathbf{x})$ , where  $A_2$  is the low-speed event  $u_L(\mathbf{x}_\times) - U < 0$  with probability  $P\{A_2\} = 0.47$  at  $\mathbf{x}_\times/\delta = (0, 0, 0.5)$ : (a) filled contours of  $|\langle \tilde{v}_L^+ | A_1 \rangle| = 0.04, 0.08, 0.12, 0.16$ ; (b) filled contours of  $|\langle \tilde{w}_L^+ | A_1 \rangle| = 0.03, 0.06, 0.09, 0.12$ ; (c) filled contours of  $|\langle \tilde{w}_L^+ | A_1 \rangle(\langle \tilde{u}_L^+ | A_1 \rangle - U^+)| = 0.02, 0.04, 0.06, 0.08$ ; and (a–c) line contours of  $|\langle \tilde{u}_S^+ | A_1 \rangle - \langle \tilde{u}_S^+ \rangle| = 0.01$ . Darker to lighter shades and dashed lines for negative values. Vectors represent in-plane velocity components. Data from snapshot of  $Re_\tau = 2k$  channel flow LES, run G1b (table 1).

large-scale streamwise and wall-normal velocities. Figures 9–11(c) show the conditioned shear stress distributions associated with the large scales, that is the product of the conditional averages of  $u_L$  and  $w_L$ . A conditionally averaged  $u_L w_L$  yields a different answer that includes the effects of smaller structures since  $\langle u_L w_L | A_1 \rangle \neq \langle u_L | A_1 \rangle \langle w_L | A_1 \rangle$ . The relative phases of  $u_L$  and  $w_L$  imply that there will be a contribution to the mean shear stress close to the wall. Note that this result is subject to the success of the conditional averaging in capturing streamwise coherence in  $u_L$  and  $w_L$ , but the trend is believed to be robust.

#### 4. Summary and Conclusions

We have designed a series of LES runs that are well-suited to the investigation of large-scale structures in a long channel. The observations from this study lend themselves to an interpretation of the ubiquitous influence of large-scale structures in turbulent chan-

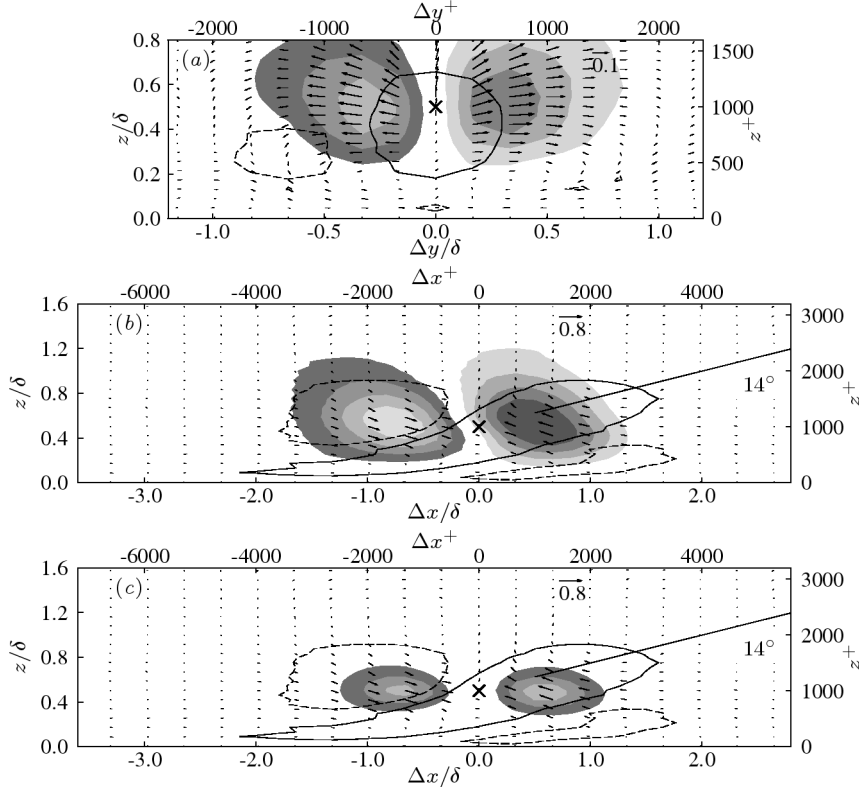


FIGURE 11. Spanwise and wall-normal velocities, and Reynolds stress associated with the conditionally averaged streamwise velocity in the (a) spanwise–wall-normal and (b, c) streamwise–wall-normal planes, with  $\langle \mathbf{u}_L^+ | A_4 \rangle (\Delta \mathbf{x})$  and  $\langle \tilde{w}_S^+ | A_4 \rangle (\Delta \mathbf{x})$ , where  $A_4$  is the streamwise high-speed-to-low-speed boundary event  $(\partial u_L / \partial x)(\mathbf{x}_\times) < 0$  with probability  $P\{A_4\} = 0.48$  at  $\mathbf{x}_\times / \delta = (0, 0, 0.5)$ : (a) filled contours of  $|\langle \tilde{v}_L^+ | A_1 \rangle| = 0.04, 0.08, 0.12, 0.16$ ; (b) filled contours of  $|\langle \tilde{w}_L^+ | A_1 \rangle| = 0.03, 0.06, 0.09, 0.12$ ; (c) filled contours of  $|\langle \tilde{w}_L^+ | A_1 \rangle (\langle \tilde{w}_L^+ | A_1 \rangle - U^+)| = 0.02, 0.04, 0.06, 0.08$ ; and (a–c) line contours of  $|\langle \tilde{u}_S^+ | A_1 \rangle - \langle \tilde{u}_S^+ \rangle| = 0.01$ . Darker to lighter shades for negative values. Vectors represent in-plane velocity components. Data from snapshot of  $Re_\tau = 2$  k channel flow LES, run G1b (table 1).

nel flow, consistent with the boundary layer experiments of Bandyopadhyay & Hussain (1984); Mathis *et al.* (2009); Guala *et al.* (2009).

Using simultaneous time and spatial data to construct the spatio-temporal spectrum, we compute the dispersion relation, and show that departure from Taylor’s frozen-turbulence hypothesis is noticeable near the wall,  $z/\delta < 0.08$ , and for large scales,  $> 6\delta$ , in channel flow at  $Re_\tau = 2$  k. This is consistent with the footprint of the very large scales reaching down to the wall. The opposite effect—that the large scales convect slower than the local mean—is also observed for these large scales away from the wall ( $z/\delta = 0.5$ ). This, too, is consistent with the conditional averages that show that these large-scale structures reach far away from the wall.

Flow fields constructed from conditional averages confirm the extent of the influence of scales with  $\lambda_x \approx 6\delta$  and reveal the wall-normal dependence of the spatial relationship between the high-speed large-scale region and the underlying small-scale intensity. The LES results appear to underline that the apparent amplitude modulation effect is better

described in terms of the spatial phase between the large and the small scales; indeed our correlation coefficients,  $R_\rho$  and  $R_\tau$ , are formulated in terms of this phase relationship. In this context, the zero in the correlation between large and small scale activity described in § 3.2 can be interpreted as the location where, on average, the corresponding signals are  $\pi/2$  out of phase. A picture emerges in which the small scales are nominally in phase with the large scales near the wall and  $\pi$  out of phase further from the wall. In the intervening region, where the phase difference is approximately  $\pi/2$ , the small scales track the sign of  $\partial u_L/\partial x$ , per the small-scale production/backscatter term  $-2\tilde{u}_S^2\partial u_L/\partial x$ . We can interpret the small scale activity,  $\tilde{u}_S$ , in terms of local structure, noting that the inferred locus of the maximum small scale energy corresponds to the well-known structure inclination angle of approximately  $10\text{--}20^\circ$ , at least at this Reynolds number.

We conclude by observing that the very large scales appear to dictate some of the turbulence behavior close to the wall, with interesting implications for the “top-down versus bottom-up” debate concerning the dynamical significance of different regions of the flow. It is perhaps more correct to say simply that the two regions can now be determined to be inextricably linked.

The authors acknowledge the support of the NSF under grants CBET-0651754 (D.C.) and CAREER-0747672 (B.J.M.). It is our pleasure to acknowledge Professor D. I. Pullin’s generous support for this investigation, and useful discussions with Drs. Ati Sharma and Michele Guala.

## REFERENCES

- BANDYOPADHYAY, P. R. & HUSSAIN, A. K. M. F. 1984 The coupling between scales in shear flows. *Phys. Fluids* **27**, 2221–2228.
- CANTWELL, B. J. 1981 Organized motion in turbulent flow. *Ann. Rev. Fluid Mech.* **13**, 457–515.
- CHAPMAN, D. R. 1979 Computational aerodynamics, development and outlook. *AIAA J.* **17**, 1293–1313.
- CHUNG, D. & PULLIN, D. I. 2009 Large-eddy simulation and wall modelling of turbulent channel flow. *J. Fluid Mech.* **631**, 281–309.
- DEL ÁLAMO, J. C., JIMÉNEZ, J., ZANDONADE, P. & MOSER, R. D. 2004 Scaling of the energy spectra of turbulent channels. *J. Fluid Mech.* **500**, 135–144.
- DENNIS, D. J. C. & NICKELS, T. B. 2008 On the limitations of Taylor’s hypothesis in constructing long structures in a turbulent boundary layer. *J. Fluid Mech.* **614**, 197–206.
- FAVRE, A. J., GAVIGLIO, J. J. & DUMAS, R. 1967 Structure of velocity space-time correlations in a boundary layer. *Phys. Fluids* **10**, S138–145.
- GUALA, M., HOMMEMA, S. E. & ADRIAN, R. J. 2006 Large-scale and very-large-scale motions in turbulent pipe flow. *J. Fluid Mech.* **554**, 521–542.
- GUALA, M., METZGER, M. J. & MCKEON, B. J. 2009 Interactions within the turbulent boundary layer at high Reynolds number. *In preparation*.
- HOYAS, S. & JIMÉNEZ, J. 2006 Scaling of the velocity fluctuations in a turbulent channels up to  $Re_\tau=2003$ . *Phys. Fluids* **18**, 011702.
- HUTCHINS, N. & MARUSIC, I. 2007a Evidence of very long meandering features in the logarithmic region of turbulent boundary layers. *J. Fluid Mech.* **579**, 1–28.
- HUTCHINS, N. & MARUSIC, I. 2007b Large-scale influences in near-wall turbulence. *Phil. Trans. R. Soc. A* **365**, 647–664.
- KIM, K. C. & ADRIAN, R. J. 1999 Very large-scale motion in the outer layer. *Phys. Fluids* **11**, 417–422.
- KOVASZNYI, L. S. G., KIBENS, V. & BLACKWELDER, R. F. 1970 Large-scale motion in the intermittent region of a turbulent boundary layer. *J. Fluid Mech.* **41**, 283–325.
- KROGSTAD, P.-Å., KASPERSEN, J. H. & RIMESTAD, S. 1998 Convection velocities in a turbulent boundary layer. *Phys. Fluids* **10** (4), 949–957.

- MARUSIC, I. & HEUER, W. D. C. 2007 Reynolds number invariance of the structure inclination angle in wall turbulence. *Phys. Rev. Lett.* **99**, 114504.
- MATHIS, R., HUTCHINS, N. & MARUSIC, I. 2009 Large-scale amplitude modulation of the small-scale structures in turbulent boundary layers. *J. Fluid Mech.* **628**, 311–337.
- MISRA, A. & PULLIN, D. I. 1997 A vortex-based subgrid stress model for large-eddy simulation. *Phys. Fluids* **9**, 2443–2454.
- MONTY, J. P. & CHONG, M. S. 2009 Turbulent channel flow: comparison of streamwise velocity data from experiments and direct numerical simulation. *J. Fluid Mech.* **633**, 461–474.
- MONTY, J. P., HUTCHINS, N., NG, H. C. H., MARUSIC, I. & CHONG, M. S. 2009 A comparison of turbulent pipe, channel and boundary layer flows. *J. Fluid Mech.* **632**, 431–442.
- MONTY, J. P., STEWART, J. A., WILLIAMS, R. C. & CHONG, M. S. 2007 Large-scale features in turbulent pipe and channel flows. *J. Fluid Mech.* **589**, 147–156.
- MORRISON, J. F., MCKEON, B. J., JIANG, W. & SMITS, A. J. 2004 Scaling of the streamwise velocity component in turbulent pipe flow. *J. Fluid Mech.* **508**, 99–131.
- REYNOLDS, W. C. & HUSSAIN, A. K. M. F. 1972 The mechanics of an organized wave in turbulent shear flow. part 3. theoretical models and comparisons with experiments. *J. Fluid Mech.* **54**, 263–288.
- VOELKL, T., PULLIN, D. I. & CHAN, D. C. 2000 A physical-space version of the stretched-vortex subgrid-stress model for large-eddy simulation. *Phys. Fluids* **12**, 1810–1825.
- WILLS, J. A. B. 1964 On convection velocities in turbulent shear flows. *J. Fluid Mech.* **20**, 417–432.